Synthesis and Characterization of AB_2O_4 (A=Fe, Ni, Mn; B=Fe) Magnetic Nanoparticles

A Dissertation Submitted in the Partial Fulfillment
of Requirement for the Award of the
Degree of

Masters of Science
in
Physics

Submitted by

Navpreet Kaur
(Roll no.-301004010)

Under the supervision of

Dr. B N Chudasama

Assistant Professor & Research Supervisor
School of Physics and Materials Science
Thapar University
Patiala (Punjab)-147 004

July 2012

Dedicated to...

Almighty GOD and my Family

Certificate

This is to certify that the dissertation entitled **"Synthesis and Characterization of AB_2O_4 (A=Fe, Ni, Mn; B=Fe) Magnetic Nanoparticles"** submitted by **Ms. Navpreet Kaur** (Roll No.301004010) of M.Sc. (Physics), Thapar University, Patiala was carried out by her under my supervision. The work presented in this thesis is her own work and is not credit towards any other degree at Thapar University, Patiala or any other University.

(Dr. Bhupendrakumar Chudasama)

Assistant Professor & Research Supervisor
School of physics and Materials Science
Thapar University
Patiala-147004

(Dr. Kulvir Singh)

Associate Professor and Head
School of physics and Materials Science
Thapar University
Patiala

(Dr. S.K. Mohapatra)

Dean of Academic Affairs
Thapar University
Patiala

Acknowledgement

With deep sense of gratitude, I would like to express my sincere thanks to all those who gave me the possibility to complete thesis dissertation work.

First of all, I want to thanks my supervisor, Dr B N Chudasama, Assistant Professor, Thapar University, Patiala. He is always willing to listen, discuss and advice throughout the work. The encouragement and guidance from him is always appreciated. Thanks are also due to Dr. Nidhi Andhariya, for useful discussions and helpful feedbacks. I am sure that the knowledge gained through my association with her shall go a long way in helping me to achieve the success in my life.

I would like to express my sincere regards to Dr. Kulvir Singh, Head, School of Physics and Materials Science for providing me necessary infrastructural facilities for carrying out this work.

I would like to thank Miss Chandni and my friends who have been a constant source of support. Last but not the least; I would like to thank my Father, S. Surinder Pal Singh, Mother Mrs. Parminder Kaur and Brother Mr. Abhitej Singh for their love and encouragement. This work would not have been possible without them.

Navpreet Kaur

Ms. Navpreet Kaur

ABSTRACT

This dissertation deals with the Synthesis and Characterization of AB_2O_4 magnetic nanoparticles where A and B are defined as A=Fe, Mn, Ni; B=Fe. The magnetic nanoparticles were prepared by the chemical co-precipitation technique. Magnetic nanoparticles of Fe_3O_4, $MnFe_2O_4$, $NiFe_2O_4$ were characterized by X-ray diffraction (XRD), UV-visible spectroscopy, Transmission electron microscopy (TEM) and Dynamic light scattering (DLS).The synthesized magnetic nanoparticles of Fe_3O_4, $MnFe_2O_4$ and $NiFe_2O_4$ have the cubic inverse spinel structure. The average crystallite size of Fe_3O_4, $MnFe_2O_4$, $NiFe_2O_4$ nanoparticles were 8.40 nm, 9.60 nm and 8.25 nm, respectively. The morphological study from TEM microscopy revealed that the Fe_3O_4 nanoparticles are polydisperse in nature with near spherical morphology. The band gap values were calculated from UV-visible spectral analysis. Hydrodynamic size and its distribution were determined by DLS. The Hydrodynamic size of Fe_3O_4, $MnFe_2O_4$, $NiFe_2O_4$ nanoparticles were 23.5 nm, 22.0 nm and 21.4 nm, respectively and the polydispersity indices are 0.036,0.065 and 0.133, respectively.

CONTENTS **PAGE NUMBER**

LIST OF FIGURES

LIST OF TABLES

Chapter 1 Introduction

1.1Nanotechnology

Nanotechnology manipulates matter at the atomic, molecular and macromolecular level to create and control objects on the nanometre scale, with the goal of fabricating novel materials, devices and systems that have new properties and functions because of their small size [1]. It deals with materials having at least one dimension between 1 to 100 nm and involves developing materials or devices within that size [2]. Nanotechnology is considered as a key technology for the future.

How small is "nano"? A nanometer is one billionth or 10^{-9} of a meter. A sheet of paper is about 100,000 nm thick. And there are 25,400,000 nm in one inch .By comparison, typical carbon-carbon bond lengths, or the spacing between these atoms in a molecule, are in the range 0.12–0.15 nm, and a DNA double-helix has a diameter around 2 nm. On the other hand, the smallest cellular life-forms, the bacteria of the genus Mycoplasma, are around 200 nm in length. Since nanotechnology must build its devices from atoms and molecules, therefore the lower limit is set by the size of atoms. The upper limit is more or less arbitrary but is around the size that phenomena not observed [3]. Encompassing nanoscale science, engineering, and technology, nanotechnology involves imaging, measuring, modeling, and manipulating matter at this length scale.

We are interested in the nanoscale because materials reduced to the nanoscale can show different properties compared to what they exhibit on a macro scale, enabling unique applications. Matter such as gases, liquids, and solids can exhibit unusual physical, chemical, and biological properties at the nanoscale. For instance, opaque substances become transparent (copper); stable materials turn combustible (aluminium); insoluble materials become soluble (gold), etc. Some nanostructured materials are stronger or have different magnetic properties compared to other forms or sizes of the same material. They may become more chemically reactive or reflect light better or change colour as their size or structure is altered. Much of the fascination with nanotechnology stems from these quantum and surface phenomena that matter exhibits at the nanoscale [4].

1.2 Magnetism

Magnetism is a force of attraction or repulsion that acts at a distance. It is due to a magnetic field, which is caused by moving electrically charged particles [5]. When a charged particle moves, it creates a magnetic field around its path.

1.3 Types of Magnetism

All magnetic materials contain magnetic moments, which behave in a way similar to microscopic bar magnets. The magnetic behaviour of materials can be classified into the following five major groups:

1. Diamagnetism

2. Paramagnetism

3. Ferromagnetism

4. Ferrimagnetism

5. Antiferromagnetism

Materials in the first two groups are those that exhibit no collective magnetic interactions and are not magnetically ordered. Materials in the last three groups exhibit long-range magnetic order below a certain critical temperature. Ferromagnetic and ferrimagnetic materials are usually what we consider as being magnetic (i.e., behaving like iron). The remaining two are so weakly magnetic that they are usually thought of as "nonmagnetic".

1.3.1Diamagnetism

Diamagnetism appears in all materials, and is the tendency of a material to oppose an applied magnetic field, and therefore, to be repelled by a magnetic field. However, in a material with paramagnetic properties (that is, with a tendency to enhance an external magnetic field), the paramagnetic behaviour dominates [6]. Thus, despite its universal occurrence, diamagnetic behaviour is observed only in a purely diamagnetic material. In a diamagnetic material, there are no unpaired electrons, so the intrinsic magnetic moments cannot produce any bulk effect.

The magnetic susceptibility (χ) of a diamagnetic substance is negative and of the order of 10^{-5}. There is no appreciable variation of diamagnetism with temperature. In the absence of applied magnetic field, each atom has net zero magnetic moment. In the presence of an applied magnetic field, the angular velocities of the electronic orbits are changed. These induced magnetic dipole moments align themselves opposite to the applied field. Water, Gold, Bismuth, Copper, Zinc, Mercury are examples of diamagnetic materials.

1.3.2 Paramagnetism

In a paramagnet, the magnetic moments tend to be randomly orientated due to thermal fluctuations when there is no magnetic field as shown in figure 1.1. In an applied magnetic field these moments start to align parallel to the field such that the magnetisation of the material is proportional to the applied field. Paramagnetic materials such as liquid oxygen and aluminium show a weak magnetic attraction when placed near a magnet. Some atoms or ions in the material have a net magnetic moment due to unpaired electrons in partially filled orbitals. In the presence of a field, there is partial alignment of the atomic magnetic moments in the direction of the field resulting in a net positive magnetisation and positive susceptibility.

In strong magnetic field, paramagnetic materials become magnetic and will stay magnetic while the field is present. When the strong magnetic field is removed the net magnetic alignment is lost and the magnetic dipoles relax to a random position [7].

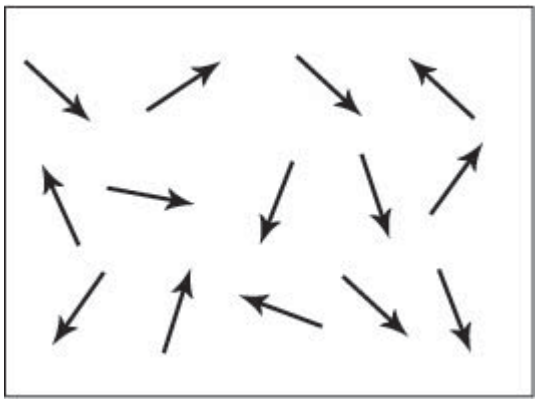

Figure 1.1: Schematic showing the magnetic dipole moments randomly aligned in a paramagnetic sample

1.3.3 Ferromagnetism

Magnetic moments in a ferromagnet have the tendency to aligned parallel to each other under the influence of a magnetic field as shown in figure 1.2. However, unlike the moments in a paramagnet, these moments will then remain parallel when a magnetic field is not applied.

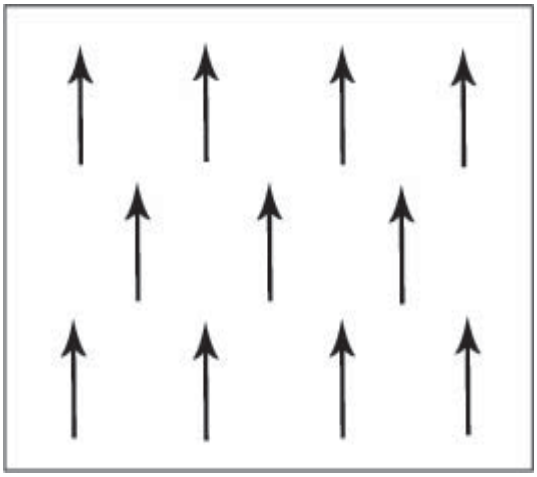

Figure 1.2: Schematic showing the magnetic dipole moments aligned parallel in a ferromagnetic material.

The atomic moments in these materials exhibit very strong interactions. These interactions are produced by electronic exchange forces and result in a parallel or antiparallel alignment of atomic moments. Exchange forces are very large, equivalent to a field on the order of 1000 Tesla, or approximately a 100 million times the strength of the earth's field. The exchange force is a quantum mechanical phenomenon due to the relative orientation of the spins of two electrons. The elements Fe, Ni, and Co and many of their alloys are typical ferromagnetic materials.

1.3.4 Antiferromagnetism

Adjacent magnetic moments from the magnetic ions tend to align anti-parallel to each other without an applied field. In the simplest case, adjacent magnetic moments are equal in magnitude and opposite therefore there is no overall magnetisation. The magnetic moment orientation in an antiferromagnetic material is shown in figure 1.3.

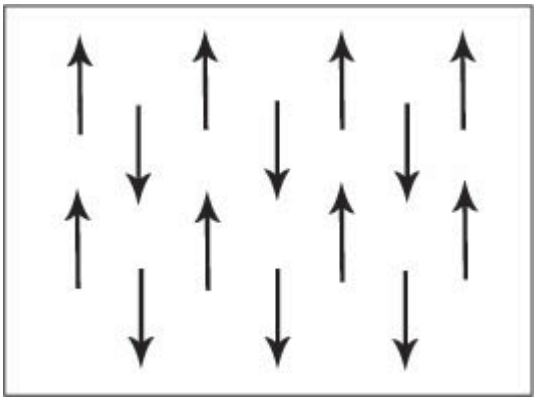

Figure 1.3: Schematic showing adjacent magnetic dipole moments with equal magnitude aligned anti-parallel in an antiferromagnetic material.

1.3.5 Ferrimagnetism

The aligned magnetic moments are not of the same size; i.e. more than one type of magnetic ions present. An overall magnetisation is produced but not all the magnetic moments may give a positive contribution to the overall magnetisation. Ferrimagnetic materials have two sets of magnetic dipole moments pointing in opposite directions. The magnetic moments do not cancel each other out because the dipole moment in one direction is smaller than the other. Figure 1.4 shows the magnetic moments of different magnitudes aligned anti-parallel.

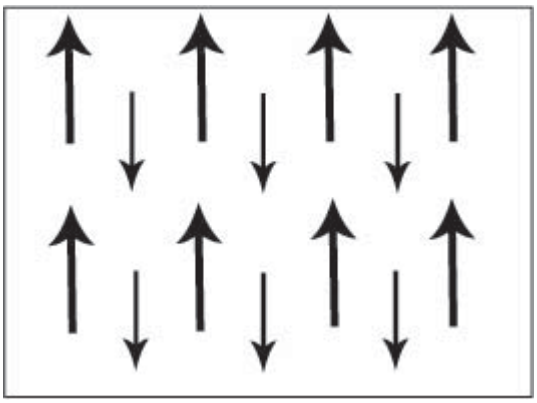

Figure 1.4: Schematic showing adjacent magnetic moments of different magnitudes aligned anti-parallel.

1.4 Magnetism at nanoscale

Magnetism in materials at nanoscale is very fascinating. The magnetic properties of nanomaterials differ substantially from the bulk counterparts. This is due to

1. Surface effects

2 Finite size effects [8]

1.4.1 Surface effects

As the particle size decreases, a large percentage of atoms in a nanoparticle are on the surface, which implies that surface and interface effects become more important. For example, for face-centered cubic (fcc) cobalt with a diameter of around 1.6 nm, about 60 % of the total numbers of spins are surface spins [9]. Owing to this large surface atoms/bulk atoms ratio, the surface spins make an important contribution to the magnetization. This local breaking of the symmetry might lead to changes in the band structure, lattice constant or/and atom coordination. Under these conditions, some surface and/or interface related effects occur, such as surface anisotropy and, under certain conditions, core–surface exchange anisotropy can occur.

Surface effects can lead to a decrease of the magnetization of small particles, for instance oxide nanoparticles, with respect to the bulk value. This reduction has been associated with different mechanisms, such as the existence of a magnetically dead layer on the particle's surface; the existence of a spin-glass-like behaviour of the surface spins [10]. On the other hand, for small metallic nanoparticles, for example cobalt, an enhancement of the magnetic moment with decreasing size was reported as well.

A principal effect of finite size on a magnetic particle is the breaking of a large number of exchange bonds for surface atoms. This can have a particularly strong effect on ionic materials, since the exchange interactions are largely antiferromagnetic, super exchange [11] interactions. This interaction is an indirect exchange mechanism whereby electrons are shared between 3d orbitals of the metal ions and 2p orbitals of the oxygen ions. The interaction strength is proportional to the overlap between these orbitals; hence it depends on the bond length and angle between the metal ions and the intervening oxygen ion. In bulk spinel ferrites MFe_2O_4(M=Ni, Co, Mn, etc.) the division of the 24 cationic sites in the unit cell into two magnetic sub lattices is the result of a balance between competing antiferromagnetic interactions. When some exchange bonds are removed at the surface, there can be frustration and spin disorder [12].

1.4.2 Finite size effects

The two most studied finite-size effects in nanoparticles are the single-domain limit and the superparamagnetic limit. In large magnetic particles, it is well known that there is a multidomain structure, where regions of uniform magnetization are separated by domain walls. If the sample size is reduced, there is a critical volume below which it costs more energy to create a domain wall than to support the external magneto static energy (stray field) of the single-domain state. This critical diameter typically lies in the range of a few tens of nanometers and depends on the material. It is influenced by the contribution from various anisotropy energy terms.

The second important phenomenon which takes place in nanoscale magnetic particles is the superparamagnetic limit. The superparamagnetism can be understood by considering the behaviour of a well-isolated single-domain particle. The magnetic anisotropy energy per particle which is responsible for holding the magnetic moments along a certain direction can be expressed as follows $E(\theta) = K_{eff} V \sin^2\theta$,where V is the particle volume, K_{eff} is anisotropy constant and θ is the angle between the magnetization and the easy axis.[12]

1.5 Superparamagnetism

Superparamagnetism is a form of magnetism, which appears in the small ferromagnetic or ferrimagnetic nanoparticles. This phenomenon occurs when the material is composed of very small crystallites (generally, 1-10 nm). In this case even when the temperature is below the Curie or Neel temperature, the thermal energy is sufficient to change the direction of magnetization of the entire crystallite. In the absence of external magnetic field, when the time used to measure the magnetization of the nanoparticles is much longer than the Neel relaxation time, their magnetization appears to be zero: they are said to be in the superparamagnetic state. In this state, an external magnetic field is able to magnetize the nanoparticles, similarly to a paramagnet. However, their magnetic susceptibility is much larger than the paramagnets. The energy required to change the direction of magnetization of a crystallite is called the crystalline anisotropy energy and depends both on the material properties and the crystallite size. As the crystallite size decreases, so does the crystalline anisotropy energy, resulting in a decrease in the temperature at which the material becomes superparamagnetic [13].

1.6 Ferrites

Ferrites are chemical compounds consisting of ceramic materials with iron (III) oxide (Fe_2O_3) as their principal component [14]. A ferrite is formed by the reaction of ferric oxide (iron oxide or rust) with number of other metals, including magnesium, aluminium, barium, manganese, copper, nickel, cobalt, or even iron itself.

They are prepared by heat-treating the various transition metal oxides or alkaline earth oxides with the ferric oxides [15]. The magnetic behaviour exhibited by the ferrites is quite different from ferromagnetism that is exhibited by metallic materials. Ferrite exhibits ferrimagnetism due to the super-exchange interaction between electrons of metal and oxygen ions. The opposite spins in ferrite results in the lowering of magnetization compared to ferromagnetic metals where the spins are parallel. Due to the intrinsic atomic level interaction between oxygen and metal ions, ferrite has higher resistivity compared to ferromagnetic metals. This enables the ferrite to find applications at higher frequencies and makes it technologically very valuable. Their magnetic properties can greatly vary from one element to another, since the microscopic (atomic) structure is composed of two or more magnetic sub lattices.

1.7 Spinel and Inverse Spinel Structure

Spinel is an important class of mixed-metal oxides, which has the general chemical composition of AB_2O_4. Normally A is a divalent atom such as Mg, Fe, Mn, Zn, and Cu. and B is a trivalent atom such as Ti, Fe, Al, and Co. The structure consist of a cubic closed-packed array of 32 oxide ions, which forms 64 tetrahedral holes and 32 octahedral holes in one unit cell (containing eight formula units $(AB_2O_4)_8$) [16]. There are two types of sub-cells commonly described for the spinel structure, here shown in Figures 1.5-a and 1.5-b, respectively. Structure a shows the filling of 2 tetrahedral sites within one-eighth of the unit cell, and structure b shows a filled octahedral site. The arrangement of these two cubic sub-cells occurs in one unit cell. There are 12 filled octahedral sites not centered in the sub-cells that are also filled to give a total of 16 filled octahedral sites. In a normal spinel structure, all the trivalent cations are located in half the octahedral sites, while all the divalent cations occupy 1/8 of the tetrahedral sites.

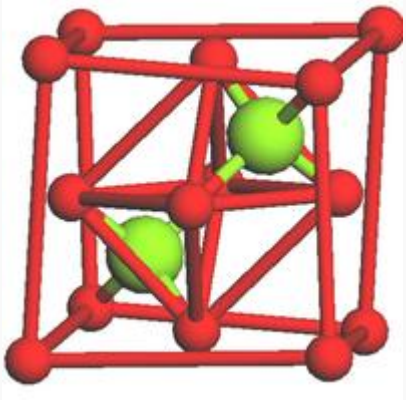

Figure 1.5 (a): Two kinds of occupied tetrahedral sites in spinel sub-cell a. A is in green and O is in red.

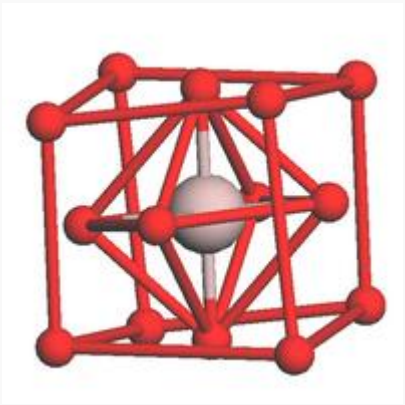

Figure 1.5(b): Occupied octahedral site in spinel sub-cell b. B is in gray, and O is in red.

The Spinel Structure

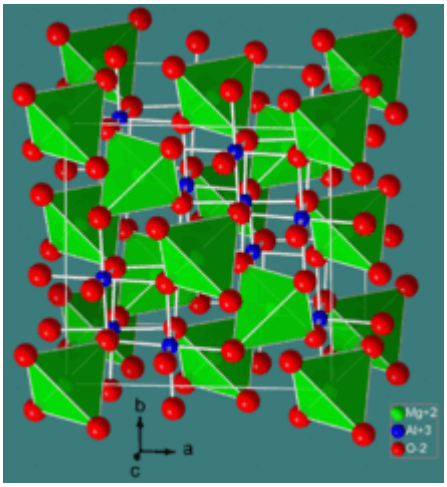

Figure 1.6: Crystal structure of spinels

Inverse spinel structures however are different in the cation distribution, in that the entire A cations and half of the B cations occupy octahedral sites, while the other half of the B cations occupies tetrahedral sites. A common example of an inverse spinel is $CoFe_2O_4$. In the case of an inverse spinel such as $CoFe_2O_4$, the Co cation occupies one half of the octahedral coordination sites [17]. Half of the Fe^{3+} cation occupies the other half of the octahedral coordination sites as well as all of the tetrahedral coordination sites. The crystal structure of $CoFe_2O_4$ is shown in Figure 1.7.

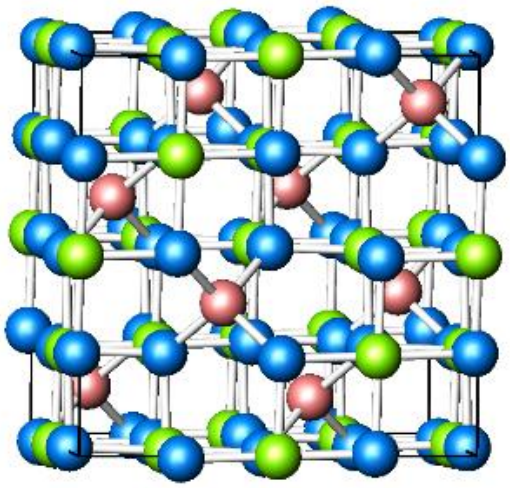

Figure 1.7: Crystal Structure of $CoFe_2O_4$ where green atoms are Co, pink atoms are Fe, and blue atoms are O

In order to explain the adoption of a particular cation distribution in a spinel structure, one must take into account the crystal field stabilization energies of the transition metals present. Some ions may have a distinct preference on the octahedral site which is dependent on the d-electron count. If the A^{2+} ions have a strong preference for the octahedral site, they will force their way into it and displace half of the B^{3+} ions from the octahedral sites to the tetrahedral sites. If the B^{3+} ions have a low or zero octahedral site stabilization energy, then they have no preference and will adopt the tetrahedral site. There is a tendency of formation of inverse spinel structure in some cases (not all the cases) which contain transition metal ions. This is because, the transition metal ion may get extra stability in octahedral geometry, prefers octahedral voids over tetrahedral ones.

Parvin et al. [18] reported the synthesis of the monodisperse Fe_3O_4 nanoparticles by reaction of iron acetylacetonate in phenyl ether at high temperature. A blocking temperature of T_b 520 K was determined by magnetization measurements on powder samples. Above T_b the nanoparticles show superparamagnetic behaviour and the particle diameter was obtained from Langevin function i.e. 4 nm which were similar to the results obtained from XRD. The nanoparticles shows ferromagnetic behaviour when temperature is below T_b and coercive field of 400 Oe at 2.5 K was applied and temperature come close to clocking temperature as field goes to zero.

Jing et al. [19] reported the synthesis and characterization of biocompatible Fe_3O_4 nanoparticles with a size range of 8–20 nm which were prepared by the modified controlled chemical coprecipitation method from the solution of ferrous/ferric mixed salt-solution in alkaline medium. Sodium oleate was chosen as the apt surfactant to achieve ultrafine, nearly spherical and well-dispersed (water-base) Fe_3O_4 nanoparticles, which had suitable magnetic properties. The effect of many parameters on the Fe_3O_4 nanoparticles was studied, such as reaction temperature, pH of the solution, stirring rate and concentration of sodium oleate which showed that the Fe_3O_4 nanoparticles can be produced in the sizes ranged from 8 to 20 nm.The biocompatibility of magnetite nanoparticles was determined by 5-dimethylthiazol-2-yl-2,5- diphenyltetrazolium bromide (MTT) assay. The saturation magnetization of magnetite nanoparticles increased from 41.60 to 49.24 emu/g, and the magnetic field intensity for the magnetite nanoparticles was in the range 8000 – 15,000 Oe. The results showed that the Fe_3O_4 nanoparticles coated by sodium oleate had a better biocompatibility, better magnetic properties, easier washing, lower cost, and better dispersion than the magnetite nanoparticles coated by PEG.

Wu et al. [20] reported the synthesis of Fe_3O_4 magnetic nanoparticles by ultrasonic –assisted chemical co-precipitation technique utilizing high purity iron separated from iron ore tailings by acidic leaching method. X-ray diffraction, field-emission scanning electron microscopy and vibrating sample magnetometer determined the magnetite particles with 15 nm average diameter. Fe_3O_4 particles exhibited super-paramagnetic behaviour, and $C_{12}H_{25}OSO_3Na$ was added as surface active agent, assisting to obtain Fe_3O_4 nanoparticles with uniform size and

shape distribution. The product consisted of ferrous ferrite (Fe_3O_4) nanosized cubic particles with a high level of crystallinity and exhibit super-paramagnetism.In the present study nanoparticles synthesis do not requires any protecting gas.

Kang et al. [21] presented the direct synthesis of highly crystalline and monodisperse manganese ferrite nanocrystals via the thermal decomposition of metal-surfactant complexes followed by mild chemical oxidation. On changing the experimental parameters particle sizes could be varied from 5 to 13 nm. The regularity of the nanocrystals was demonstrated by the formation of two and three-dimensional super lattices. The high crystallinity of the manganese ferrite nanocrystals was analyzed by Electron diffraction, X-ray diffraction, and high-resolution TEM images. Elemental analysis and energy-dispersive X-ray spectroscopy confirmed that the molar ratio of Mn: Fe was 1:2. The nanocrystals were found to exhibit the typical behaviours of magnetic nanocrystals with the characteristic narrow energy barrier distributions of magnetic anisotropy, confirming the uniformity of the nanocrystals.

Chinnasamy et al. [22] reported the size dependent magnetic properties and cation inversion in chemically synthesized $MnFe_2O_4$ nanoparticles. A pure phase spinel ferrite structure for all samples was revealed by X-ray diffractograms. Transmission electron microscopy showed that the particles consist of a mixture of both spherical (smaller) and cubic (larger) particles dictated by the reaction kinetics. High temperature magnetometry measured the Neel temperatures (T_N) of $MnFe_2O_4$ for various particle sizes. 4 nm $MnFe_2O_4$ particles showed a T_N of about 320 °C whereas the 50 nm particles had a T_N of about 400 °C. The high Neel temperature, compared with the bulk $MnFe_2O_4$ T_N of 300 °C, is due to a change in cation distribution between the tetrahedral and octahedral sites of the spinel lattice. Results of extended x-ray absorption fine structure measurements indicate a systematic change in the cation distribution dependent on processing conditions.

Mozaffari et al. [23] presents the preparation and characterization of manganese ferrite nanoparticles via co-precipitation method for hyperthermia. X-ray diffraction method analysed the phase identification of the nanopowders and the mean particle size of the nanopowders was calculated by Scherrer's formula, using necessary corrections .Vibrating sample magnetometer measured the magnetic parameters of the prepared nanopowders. A sensitive thermometer was used to measure the increase in temperature due to application of an alternating magnetic field on suspended magnetic nanopowders in water. Transmission

electron microscope investigations showed that the particle size distribution was homogeneous and their size was in a good agreement with those obtained by Scherrer's formula. The results revealed that a single phase Mn ferrite can be obtained by co-precipitation method at 70 °C with a mean particle size of 5 nm and a 5 °C temperature increase is achievable in an AC magnetic field.

Jamil et al. [24] presented the microwave assisted synthesis of fine magnetic manganese ferrite particles using co-precipitation technique. The manganese ferrite has been synthesized using $MnCl_2.4H_2O$, $FeCl_3.6H_2O$ and NaOH via the standard co-precipitation route. Different effects were studied such as effect of concentrations, effect of duration on digestion and digestion temperature on the structural properties of the particles. In the formation of Mn ferrite an increase of pH value up to 12.5 accelerated the formation of the ferrite, but a further increase of pH up to 14 led to a reduction of the ferrite yield. The solutions were then oven dried or treated with microwaves. The ferrite phase of the particles was determined by the powder X-ray diffraction technique. The particle size was calculated by Scherer's formula using the broadening of the characteristic (311) peak of the spinel ferrite in the range of 18.7-23.9 nm. It has been concluded that below 80°C, the particles are in irregular shape and clustered. On treating such particles with microwave, the crystallinity of the particles was improved. Microwave treated particles are spherical, well dispersed and the particle size is almost uniform. Microwave treated particles have significant spinel phase as compared to the oven treated particles from XRD patterns. It also indicates that particles after the microwave treatment have better crystallinity than oven treated particles.

Shafi et al. [25] reported the synthesis of nanosized amorphous $NiFe_2O_4$ powder by sonochemical decomposition of solutions of volatile organic precursors, $Fe(CO)_5$ and $Ni(CO)_4$, in decalin at 273 K, under an oxygen pressure of 100-150 kPa.Various techniques, such as SEM, TEM, electron diffraction and X-ray diffractograms confirmed the amorphous nature of these particles. Magnetic data, Mossbauer, and EPR spectral studies indicate the superparamagnetic nature of the as-prepared amorphous and also the ultrafine nature of the crystallized sample. Saturation magnetization of the annealed sample (25 emu/g) was significantly lower than that for the reported multidomain bulk particles (55 emu/g), reflecting the ultrafine nature of the sample. Thermo gravimetric measurements with a permanent magnet gave Curie temperatures of 440 °C for amorphous and 560 °C for the crystallized forms.

Zhou et al. [26] reported the nanocrystalline nickel ferrite ($NiFe_2O_4$) particles were successfully synthesized in situ in an amorphous silica matrix by mechanical activation at room temperature. The phase development in the amorphous precursors, derived via a modified sol–gel synthesis route, with increasing mechanical activation time was analyzed by transmission electron microscopy, X-ray diffraction, and Raman spectroscopy. $NiFe_2O_4$ nanoparticles of 8.05 nm in mean particle size with a standard deviation of 1.24 nm, which were well dispersed in the silica matrix, were realized by 30 h of mechanical activation. The phase formation of nanocrystalline $NiFe_2O_4$ particles involves the nucleation of Fe_3O_4 in amorphous silica at the initial stage of mechanical activation, and the subsequent incorporation of Ni^{2+} into Fe_3O_4 forming $NiFe_2O_4$ .Their magnetic anisotropy, surface spin disorder, and cation distribution are investigated by considering both the strain imposed by silica matrix and the buffer effect during mechanical activation.

Nejati et al. [27] reported the synthesis of $NiFe_2O_4$ nanoparticles by the hydrothermal method and the inhibition of surfactant (Glycerol or Sodium dodecyl sulfate) on the particles growth was also investigated. The results showed that with increasing temperature, the crystallinity of nanoparticles was increased. The results of XRD and ICP-AES showed that the products were pure $NiFe_2O_4$ and also nanoparticles grow with increasing the temperature, while surfactant prevents the particle growth under the same condition. The average particle size was determined from the Scherrer's equation and TEM micrographs and found to be in the range of 50-60 nm that decreased up to 10-15 nm in presence of surfactant. Two characteristics metal oxygen vibrational bands was showed by the FT-IR spectra. Furthermore, the saturated magnetization and coercivity of $NiFe_2O_4$ nanoparticles were in the range of 39.60 emu/g and 15.67 Qe that decreased for samples prepared in presence of surfactant. In the presence of surfactants, the crystallinity of $NiFe_2O_4$ nanoparticles decreased in comparison with surfactant- free prepared samples. Nickel ferrite nanoparticles were superparamagnetic at room temperature.

3.1 Synthesis of nanomaterials

There are two approaches to the synthesis of nanomaterials. These are:

1. Top-down approach

2. Bottom-up approach

Both approaches play very important. Schematic representation of the building up of Nanostructures is shown in figure 3.1.

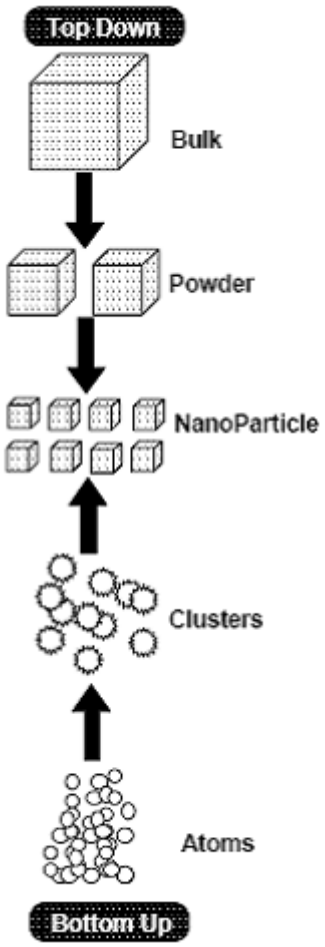

Figure3.1: Schematic representation of the building up of Nanostructures

3.1.1 Top-down approach

Top down approach refers to slicing or successive cutting of a bulk material to get nano sized particle.

Examples of top-down are:

1. Attrition or Milling
2. Etching
3. Vapour phase condensation
4. Sputtering
5. Electro-explosion
6. Laser ablation

3.1.2 Disadvantages and advantages of top-down approach

The main problem with top-down approach is the imperfection of the surface structure. The conventional top-down techniques such as lithography can cause significant crystallographic damage. Additional defects may be introduced even during the etching steps. For example, nanowires made by lithography are not smooth and may contain a lot of impurities and structural defects on surface. These imperfections would have a significant impact on physical properties and surface chemistry of nanostructures and nanomaterials, since the surface over volume ratio in nanostructures is very large. Top-down approach also introduces internal stress, in addition to surface defects and contaminations.

Despite of these disadvantages the top-down approaches continue to play a significant role in the synthesis and fabrication of nanostructures because they are economical and mass scale production is possible with these methods.

3.1.3 Bottom-up approach

Bottom up approach refers to the build up of a material from the bottom: atom by atom, or molecule by molecule or cluster by cluster.

Examples of bottom –up approach are:

1. Colloidal dispersion

2. Nanolithography and nano manipulation
3. Micro-emulsion
4. Sol-gel
5. Reverse micelle
6. Chemical co-precipitation

3.1.4 Advantages and disadvantages of bottom-up approach

Although the bottom-up approach is nothing new, it plays an important role in the fabrication and processing of nanostructures and nanomaterials. There are several reasons for this. When structures fall into a nanometer scale, there is little choice for a top-down approach. All the tools we have possessed are too big to deal with such tiny subjects. Bottom-up approach also promises a better chance to obtain nanostructures with less defects, more homogeneous chemical composition, and better short and long range ordering. This is because the bottom-up approach is driven mainly by the reduction of Gibbs free energy, so that nanostructures and nanomaterials produced by these methods are in a state which is close to a thermodynamic equilibrium.

3.1.5 Chemical coprecipitation

In chemistry, coprecipitation is the process in which precipitate of substances normally soluble under the conditions employed is achieved [28]. There are three main mechanisms of coprecipitation: inclusion, occlusion, and adsorption [29]. An inclusion occurs when the impurity occupies a lattice site in the crystal structure of the carrier, resulting in a crystallographic defect; this can happen when the ionic radius and charge of the impurity are similar to those of the carrier. An adsorbate is an impurity that is weakly bound (adsorbed) to the surface of the precipitate. An occlusion occurs when an adsorbed impurity gets physically trapped inside the crystal as it grows.

Coprecipitation is used as a method of magnetic nanoparticles synthesis.[30]Co-precipitation is a facile and convenient way to synthesize iron oxides (either Fe_3O_4 or γ-Fe_2O_3) from aqueous Fe^{2+}/Fe^{3+} salt solutions by the addition of a base under inert atmosphere at room temperature or at elevated temperature. The size, shape, and composition of the magnetic nanoparticles depends on the type of salts used (e.g. chlorides, sulphates, nitrates), the Fe^{2+}/Fe^{3+} ratio, the reaction temperature, the pH value and ionic strength of the media

[30].In recent years, co-precipitation approach has been used extensively to produce ferrite nanoparticles of controlled sizes and magnetic properties.[31],[32],[33],[34].

3.2 Synthesis of Fe_3O_4 nanoparticles

Co-precipitation technique has been used for the synthesis of Fe_3O_4 nanoparticles. Required quantity of aqueous solution of 0.05M $FeSO_4.7H_2O$ was mixed with 0.1M $FeCl_3.6H_2O$.The pH of the solution was maintained below 2 using dilute HCl. The molar ratio of $FeCl_3$:$FeSO_4$ was 2:1. Now 0.4 M NaOH dissolved in 100 mL distilled water was added slowly to previous mixture under constant magnetic stirring, immediately a dark precipitate was formed, which consists of nanoparticles of magnetite. The pH of solution was maintained at 10.5 using excess ammonia solution. After continuous stirring for 20 minutes at room temperature (300K); the black precipitates were magnetically decanted and washed several times with warm distilled water.

The chemical reaction takes place during synthesis is given below:

$$2FeCl_3.6H_2O + FeSO_4.7H_2O + 8NaOH \longrightarrow Fe_3O_4 + 6NaCl + Na_2SO_4 + 23H_2O$$

3.3 Synthesis of $MnFe_2O_4$ and $NiFe_2O_4$ nanoparticles

The same technique as described earlier in section 2.2 was used to obtain nanoparticles of Manganese Iron Oxide ($MnFe_2O_4$) and Nickel Iron Oxide ($NiFe_2O_4$).

The chemical reactions that take place during the synthesis for $MnFe_2O_4$ and $NiFe_2O_4$ are:

$$2FeCl_3.6H_2O + MnCl_2.4H_2O + 8NaOH \longrightarrow MnFe_2O_4 + 8NaCl + 20H_2O$$

$$2FeCl_3.6H_2O + NiCl_2.6H_2O + 8NaOH \longrightarrow NiFe_2O_4 + 8NaCl + 22H_2O$$

3.4 Characterization Techniques

As synthesized nanoparticles were characterized by the following techniques:

X-ray diffraction

UV-visible spectroscopy

Dynamic light scattering

Transmission electron microscopy

3.4.1 X-ray diffraction (XRD)

X-ray powder diffraction (XRD) is a rapid analytical technique primarily used to obtain structural information about crystalline solids and identification of different types of crystals. The material under analysis is finely ground and homogenized.

3.4.1.1 Fundamental Principles of X-ray Powder Diffraction (XRD)

X-ray diffraction is based on constructive interference of monochromatic X-rays and a crystalline sample. These X-rays are generated by a cathode ray tube, filtered to produce monochromatic radiation, collimated to concentrate, and directed toward the sample. The interaction of the incident rays with the sample produces constructive interference when conditions satisfy the Bragg's Law [35].

Bragg's law: This law relates the wavelength of electromagnetic radiation to the diffraction angle and the lattice spacing in a crystalline sample.

$$n\lambda = 2d \sin \theta$$

where d = distance between atomic layers in a crystal

λ = wavelength of the incident x-ray beam

n = integer; 1, 2, 3…first, second …order etc.

The crystal act as a series of parallel reflecting planes. Consider a ray PA incident on an atom A, and reflected in the direction "AR" from plane 1 and another ray QB reflected from atom B in the direction BS (Figure 3.2).

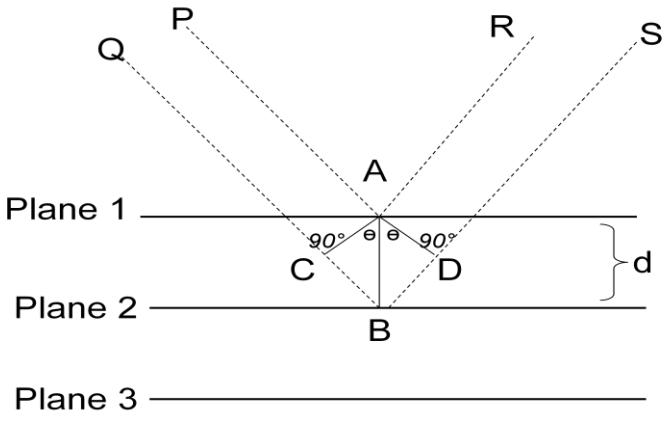

Figure 3.2: Bragg's law of reflection

The path difference between these two rays is CB+BD

The two rays will reinforce each other and produce an intense spot, when path difference is an integral multiple of wave length**.**

$CB+BD=n\lambda$

$CB=BD=d \sin\theta$

Therefore, $2d \sin\theta= n\lambda$

These diffracted X-rays are then detected, processed and counted. By scanning the sample through a range of 2θ angles, all possible diffraction directions of the lattice should be attained due to the random orientation of the powdered material.

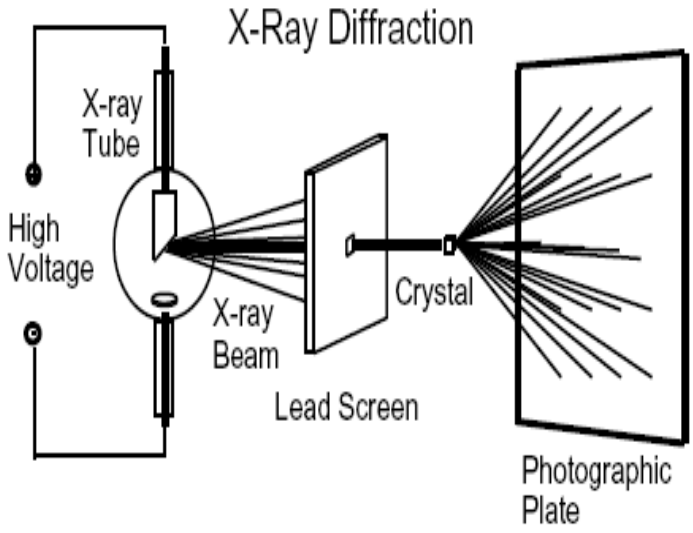

Figure 3.3: Schematic of X-ray diffraction setup

Conversion of the diffraction peaks to d-spacings allows identification of the mineral because each mineral has a set of unique d-spacings. Typically, this is achieved by comparison of d-spacings with standard reference patterns.

3.4.1.2 Uses of X-Ray Powder Diffraction

The most widespread use of X-ray powder diffraction is for the identification of crystalline compounds by their diffraction pattern. Listed below are some specific uses:

• Identification of single-phase materials – minerals, chemical compounds, ceramics or

other engineered materials.

• Determination of the crystal structure of identified materials

3.4.2Ultraviolet-visible spectroscopy

Ultraviolet and visible (UV-Vis) absorption spectroscopy measures the attenuation of a beam of light after it passes through a sample or after reflection from a sample surface. Absorption measurements can be at a single wavelength or over an extended spectral range. Ultraviolet and visible light are energetic enough to promote outer electrons to higher energy levels, and UV-Vis spectroscopy is usually applied to molecules or inorganic complexes in solution. The difference in energy between molecular bonding, non-bonding and anti-bonding orbital's ranges from 125-650 kJ/mole. This energy corresponds to EM radiation in the ultraviolet (UV) region, 100-350 nm, and visible (VIS) regions 350-700 nm of the spectrum.In this region of the electromagnetic spectrum; molecules undergo electronic transitions [36].

The UV-Vis spectra have broad features that are of limited use for sample identification but are very useful for quantitative measurements. The concentration of an analyte in solution can be determined by measuring the absorbance at specific wavelength and applying the Beer-Lambert Law.

3.4.2.1 Instrumentation

The construction of a traditional UV-VIS spectrometer is very similar to an IR spectrophotometer. Schematic representation of UV-visible spectrophotometer is shown in figure 3.4.

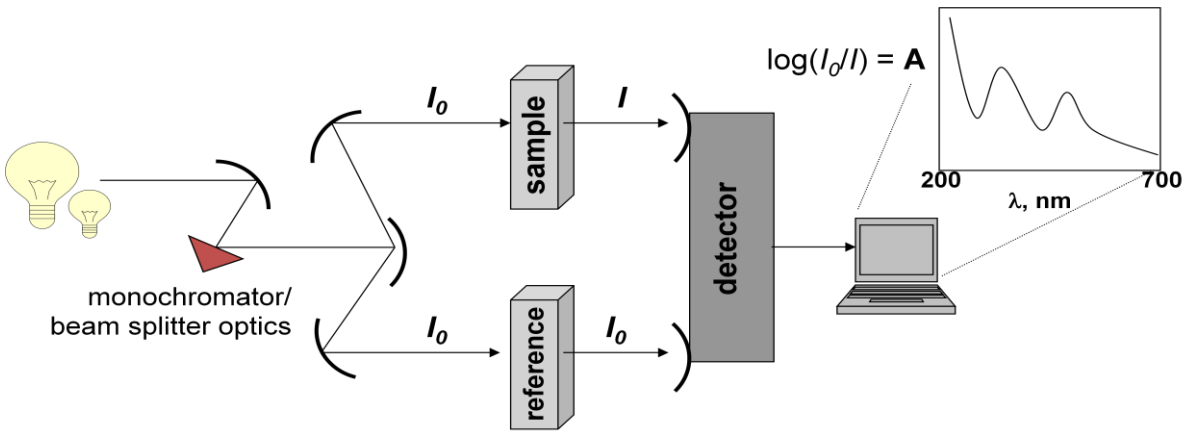

Figure 3.4: Schematic diagram of ultraviolet-visible spectrometer

Two sources are required to scan the entire UV-VIS band:

Deuterium lamp – covers the UV – 200-350

Tungsten lamp – covers 350-700

As with the dispersive IR, the lamps illuminate the entire band of UV or visible light; the monochromator (grating or prism) gradually changes the small bands of radiation sent to the beam splitter .The beam splitter sends a separate band to a cell containing the sample solution and a reference solution. The detector measures the difference between the transmitted light through the sample (I) vs. the incident light (I_0) and sends this information to the recorder.

3.4.2.2 Sample Handling

1. Virtually all UV spectra recorded are from solution-phase.
2. Cells can be made of plastic, glass or quartz.
3. Only quartz is transparent in the full 200-700 nm range; plastic and glass are only suitable for visible spectra.

Figure 3.5: A typical sample cell (commonly called a *cuvet*)

3.4.2.3 The Spectrum

The x-axis of the spectrum is in wavelength; 200-350 nm for UV, 200-700 for UV-VIS determinations.Due to the lack of any fine structure, spectra are rarely shown in their raw form, rather, the peak maxima are simply reported as a numerical list of "lambda max" values or λ_{max} .The y-axis of the spectrum is in absorbance, A. From the spectrometers point of view, absorbance is the inverse of transmittance: $A = \log_{10} (I_0/I)$. From an experimental point of

view, three other considerations must be made:

1. A longer path length, *l* through the sample will cause more UV light to be absorbed.

2. The greater the concentration, *c* of the sample, the more UV light will be absorbed

3. Some electronic transitions are more effective at the absorption of photon than others – molar absorptivity, e.

These effects are combined into the Beer-Lambert Law: $\boldsymbol{A = e\,c\,l}$

A is unit less, so the units for *e* are $cm^{-1} \cdot M^{-1}$.

3.4.2.4 Practical application of UV spectroscopy

1. UV was the first organic spectral method, however, it is rarely used as a primary method for structure determination
2. It is most useful in combination with NMR and IR data to elucidate unique electronic features that may be ambiguous in those methods
3. It can be used to assay (via λ_{max} and molar absorptivity) the proper irradiation wavelengths for photochemical experiments, or the design of UV resistant paints and coatings.
4. The most ubiquitous use of UV is as a detection device for HPLC; since UV is utilized for solution phase samples vs. a reference solvent this is easily incorporated into LC design.

3.4.3 Dynamic light scattering (DLS)

Dynamic light scattering (DLS), also known as Photon Correlation Spectroscopy (PCS) or Quasi-Elastic Light Scattering (QELS) is one of the most popular light scattering technique. It is a non-invasive, well-established technique for measuring the size of particles typically in the submicron region.

DLS is used to characterize size of various particles including proteins, polymers, micelles, carbohydrates, and nanoparticles. If the system is monodisperse, the mean effective diameter of the particles can be determined. This measurement depends on the size of the particle core, the size of surface structures, particle concentration, and the type of ions in the medium. Since DLS essentially measures fluctuations in scattered light intensity due to diffusing particles, the diffusion coefficient of the particles can be determined. DLS software

of commercial instruments typically displays the particle population at different diameters. If the system is monodisperse, there should only be one population, whereas a polydisperse system would show multiple particle populations.

3.4.3.1 Principle of Dynamic Light Scattering

The PCS method consists in analyzing the velocity distribution of particles movement by measuring dynamic fluctuations of light scattering intensity:

The disperse particles or macromolecules suspended in a liquid medium undergo Brownian motion which causes fluctuations of local concentration of the particles, resulting in local in-homogeneities of the refractive index. This in turn results in fluctuations of intensity of the scattered light. The diffusion coefficient of the particles is inversely proportional to the decay time of light scattering fluctuations. The decay time is obtained from the time-dependent correlation function of the scattered light. The particle size is calculated in accordance with Stokes-Einstein formula relating the particle size to the diffusion coefficient and viscosity.

3.4.3.2What does Dynamic Light scattering actually measure?

The diameter that is measured in Dynamic Light Scattering is called the hydrodynamic diameter and refers to how a particle diffuses within a fluid. The diameter obtained by this technique is that of a sphere that has the same translational diffusion coefficient as the particle being measured.

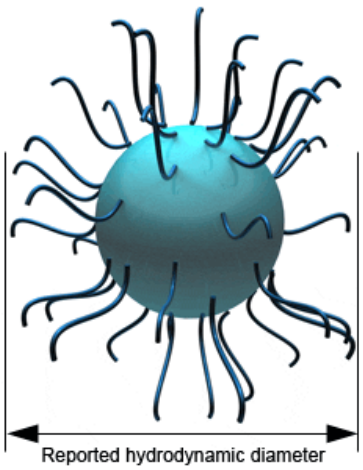

Figure 3.6: Hydrodynamic diameter of sphere

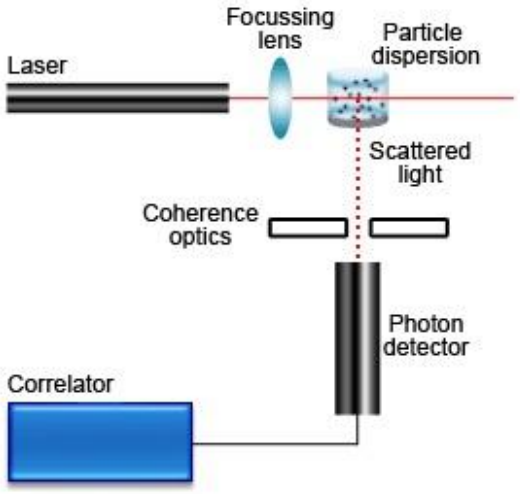

Figure 3.7: Schematic diagram of dynamic light scattering instrument

A conventional dynamic light scattering instrument is shown in figure 3.7. In most instruments, a monochromatic coherent He-Ne laser with a fixed wavelength of 633 nm is used as the light source, which converges to a waist of focus in the sample, by use of a focusing lens. Light is scattered by the particles at all angles. However, a dynamic light scattering instrument with one detector only detects the scattered light at one angle and this, historically been 90°. The intensity fluctuations of the scattered light are converted into electrical pulses, which are fed into a digital correlator. This generates the autocorrelation function, from which the appropriate data analysis is performed.

3.4.4Transmission Electron Microscope (TEM)

A Transmission Electron Microscope produces high-resolution, two-dimensional images via the interaction of electrons with a sample. TEMs are the most powerful microscopes. At a maximum potential magnification of 1 nanometer could be achieved. The transmission electron microscope (TEM) operates on the same basic principles as the light microscope but uses electrons instead of light. What you can see with a light microscope is limited by the wavelength of light. TEMs use electrons as “light source” and their much lower wavelength make it possible to get a resolution a thousand times better than with a light microscope. You can see objects to the order of a few angstroms. The possibility for high magnifications has made the TEM a valuable tool in medical, biological and materials research.

3.4.4.1 Principles of operation

The transmission electron microscope uses a high energy electron beam transmitted through a very thin sample to image and analyze the microstructure of materials with atomic scale resolution. The electrons are focused with electromagnetic lenses and the image is observed on a fluorescent screen, or recorded on film or digital camera. The electrons are accelerated at several hundred kV, giving wavelengths much smaller than that of light: 200 kV electrons have a wavelength of 0.025Å. However, whereas the resolution of the optical microscope is limited by the wavelength of light, that of the electron microscope is limited by aberrations inherent in electromagnetic lenses, to about 1-2 Å.

Because even for very thin samples one is looking through many atoms, one does not usually see individual atoms. Rather the high resolution imaging mode of the microscope images the crystal lattice of a material as an interference pattern between the transmitted and diffracted beams. This allows one to observe planar and line defects, grain boundaries, interfaces, etc. with atomic scale resolution.

3.4.4.2 Schematic diagram of transmission electron microscope

A TEM works much like a slide projector. A projector shines a beam of light through (transmits) the slide, as the light passes through it is affected by the structures and objects on the slide. These effects result in only certain parts of the light beam being transmitted through certain parts of the slide. This transmitted beam is then projected onto the viewing screen, forming an enlarged image of the slide. TEMs work the same way except that they shine a beam of electrons (like the light) through the specimen (like the slide). Whatever part is transmitted is projected onto a phosphor screen for the user to see. A more technical explanation of typical TEMs workings is as follows:

1. The "Virtual Source" at the top represents the electron gun, producing a stream of monochromatic electrons.
2. This stream is focused to a small, thin, coherent beam by the use of condenser lenses 1 and 2. The first lens (usually controlled by the "spot size knob") largely determines the "spot size"; the general size range of the final spot that strikes the sample. The second lens (usually controlled by the "intensity or brightness knob") actually changes the size of the spot on the sample; changing it from a wide dispersed spot to a pinpoint beam.

3. The beam is restricted by the condenser aperture (usually user selectable), knocking out high angle electrons (those far from the optic axis, the dotted line down the center)
4. The beam strikes the specimen and parts of it are transmitted.
5. This transmitted portion is focused by the objective lens into an image.
6. Optional Objective and Selected Area metal apertures can restrict the beam; the Objective aperture enhancing contrast by blocking out high-angle diffracted electrons. The Selected Area aperture enabling the user to examine the periodic diffraction of electrons by ordered arrangements of atoms in the sample.

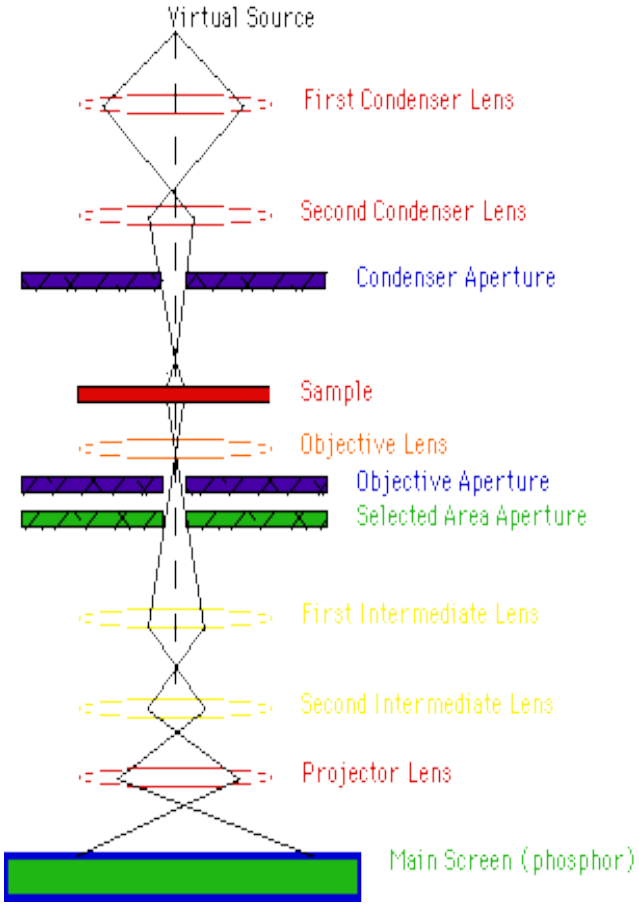

Figure 3.8: Schematic diagram of transmission electron microscope

7. The image is passed down the column through the intermediate and projector lenses.
8. The image strikes the phosphor screen, allowing the user to see the image. The darker areas of the image represent those areas of the sample that fewer electrons were transmitted through (they are thicker or denser). The lighter areas of the image represent those areas of the sample that more electrons were transmitted through (they are thinner or less dense).

4.1Structure and Phase analysis

Structural and phase investigation of magnetic nanoparticles has been carried out by powder x-ray diffraction (XRD).X-ray patterns are recorded by PANalytical X'Pert PRO MRD ML.The XRD patterns of the as-synthesized Fe_3O_4, $MnFe_2O_4$, $NiFe_2O_4$ nanoparticles are shown in figure 4.1.All the six peaks observed at 2θ~30.25^o (220), 35.75^o (311), 43.25 ^{o} (400), 53.70^o (422), 57.45^o (511) and 62.70^o (440) are indexed to a pure cubic inverse spinel structure.

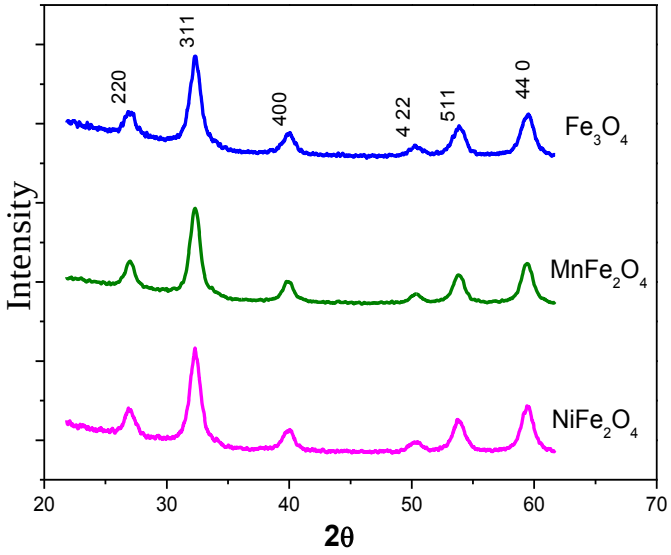

Figure 4.1: XRD pattern of Fe_3O_4, $MnFe_2O_4$,$NiFe_2O_4$ nanoparticles

The average crystallite sizes (D) of Fe_3O_4, $MnFe_2O_4$, $NiFe_2O_4$ nanoparticles has been estimated using Debye-Scherrer's Formula from the highest reflection peak in the XRD pattern [37]

$$D=0.9\lambda / \beta \cos \theta$$

Where λ is characteristics wavelength used (1.54016 A ^{o}), β is the full width at half maxima (FWHM) of highest intense peak (311), and θ is Bragg's angle. Calculated values are presented in table 1.

Table 1: Crystallite size calculated from x-ray diffraction

S.No	Sample specification	Crystallite size(nm)
1.	Fe_3O_4	8.40
2.	$MnFe_2O_4$	9.06
3.	$NiFe_2O_4$	8.25

4.2 UV-Visible Spectra study

The UV-visible spectra of Fe_3O_4, $MnFe_2O_4$, $NiFe_2O_4$ are shown in figure 4.2, 4.3 and 4.4. For UV-visible study the sample is disperse in water and it is used for the analysis. UV –visible spectra are recorded on HITACHI U-3900H Spectrophotometer.

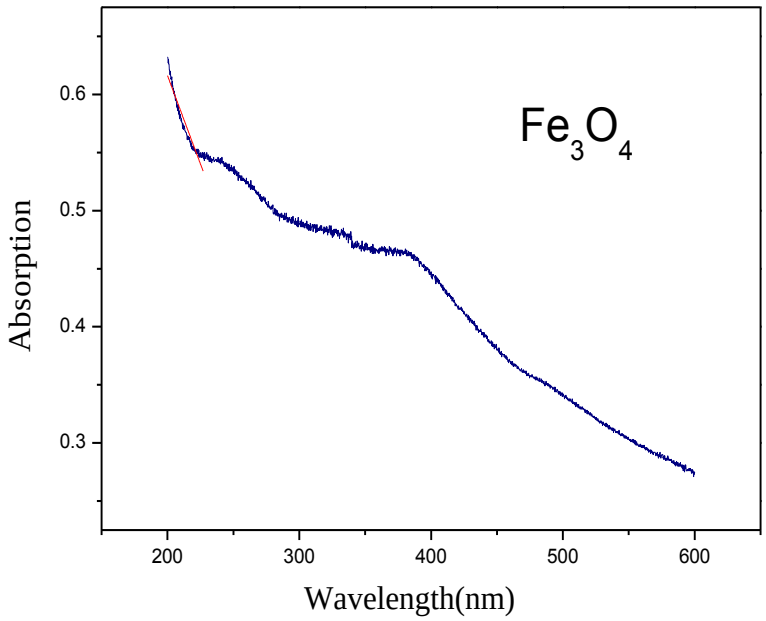

Figure 4.2: UV –visible spectrum of Fe_3O_4 nanoparticles.

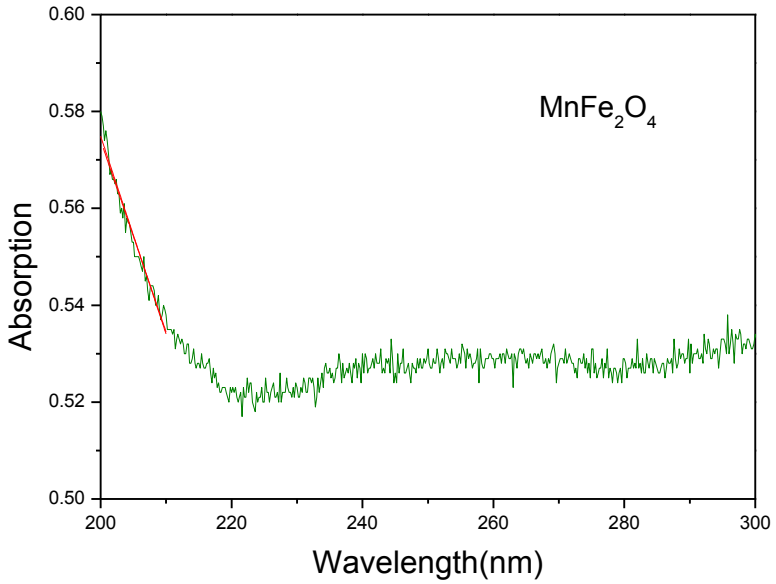

Figure 4.3: UV –visible spectrum of $MnFe_2O_4$ nanoparticles.

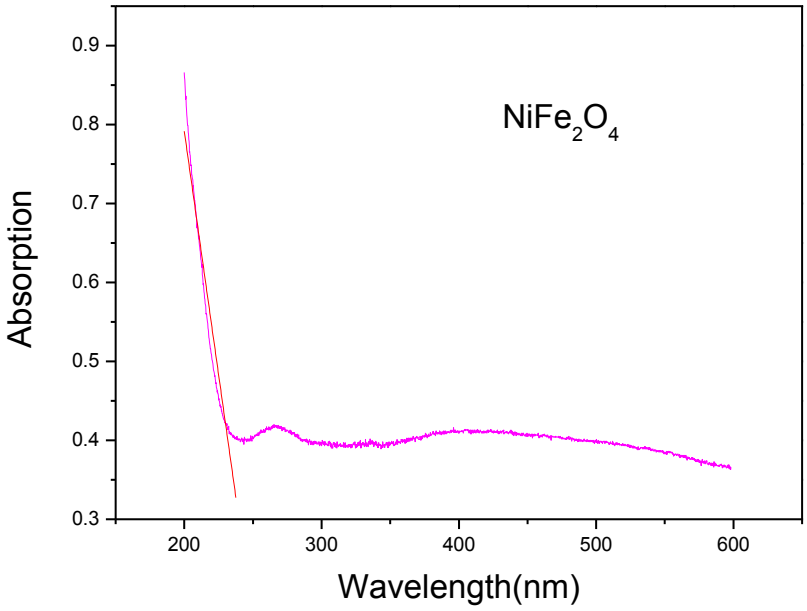

Figure 4.4: UV –visible spectrum of $NiFe_2O_4$ nanoparticles.

The band gap values of nanoparticles has been calculated using the Planck-Einstein equation

$$E=h\nu$$

Since the frequency ν, wavelength λ, and speed of light c are related by $\lambda\nu=c$, the Planck relation can also be expressed as[38]

$$\mathbf{E=h\ c\ /\ \lambda}$$

Calculated values are tabulated in table 2

Table 2: Band gap values calculated from UV-visible spectrum

S.No	Sample specification	Band gap (eV)
1.	Fe_3O_4	3.03
2.	$MnFe_2O_4$	3.58
3.	$NiFe_2O_4$	4.56

4.3Morphological study

4.3.1TEM analysis

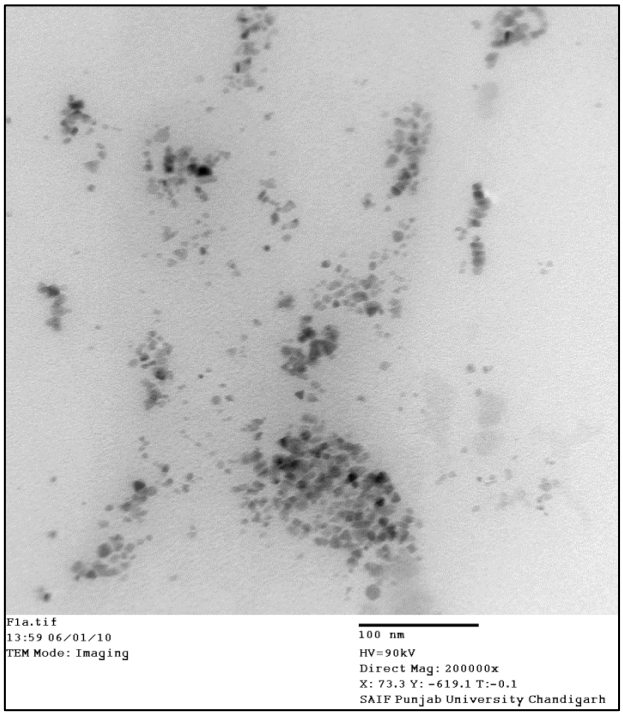

Figure 4.5: TEM micrograph of Fe_3O_4 nanoparticles

The morphological study of nanoparticles has been done by Transmission Electron Microscopy (TEM). TEM micrograph has been recorded on H7750-Hitachi model. For TEM analysis the sample is disperse in ethanol and a drop of this solution is placed on carbon coated cooper grid. Figure 4.5 shows the TEM micrograph of the Fe_3O_4 nanoparticles. It is clear from the figure that the nanoparticles are polydisperse with nearly spherical morphology. The average size of the nanoparticles is 7-18 nm with a polydispersity of 0.3 [39].

4.4 Dynamic light scattering

Dynamic light scattering (DLS) measures Brownian motion and relates this to the size of the particles. Normally DLS is concerned with measurement of particles suspended within a liquid. The larger the particle, the slower the Brownian motion will be. Smaller particles are "kicked" further by the solvent molecules and move more rapidly. The size of a particle is calculated from the translational diffusion coefficient by using the Stokes- Einstein equation;

$$d\,(H) = k\,T / 3\Pi\eta D$$

where:-

d (H) = hydrodynamic diameter

D = translational diffusion coefficient

k = Boltzmann's constant

T = absolute temperature

η = viscosity

Note that the diameter that is measured in DLS is a value that refers to how a particle diffuses within a fluid so it is referred to as a hydrodynamic diameter. [40]

The DLS technique is especially impressive because there is no sample information needed. Only the solvent viscosity and the refractive index of the solvent must be known. [41]

Particle size and polydispersity index of Fe_3O_4, $MnFe_2O_4$, $NiFe_2O_4$ nanoparticles has been determined by dynamic light scattering. The measurements were carried out on Brookhaven 90 plus particle size analyser. The size distribution histograms are presented in figure 4.6, 4.7, 4.8 and the results are tabulated in table 3.

Fe_3O_4

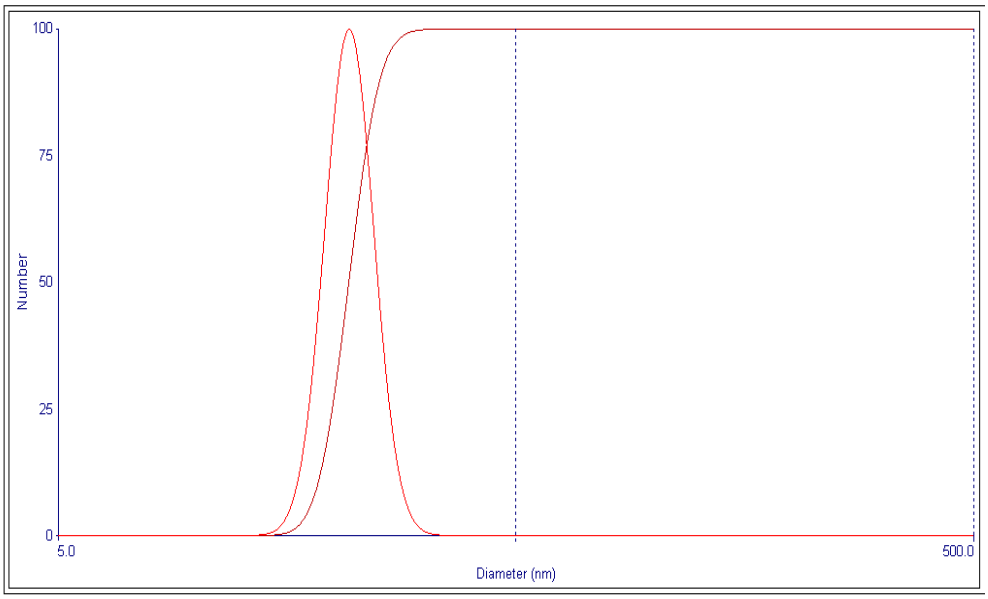

Figure 4.6: DLS of Fe_3O_4 nanoparticles

$MnFe_2o_4$

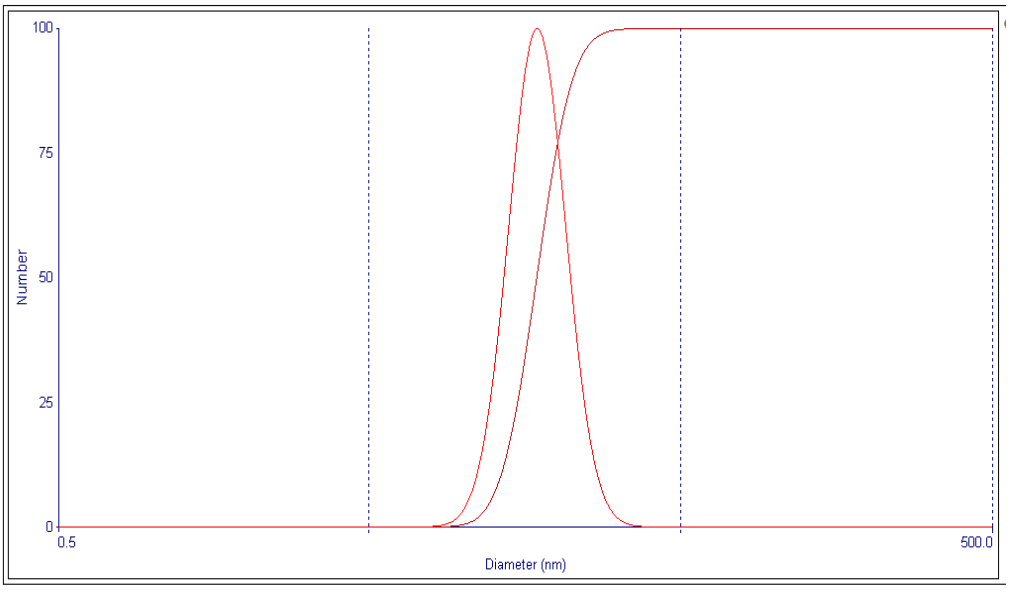

Figure 4.7: DLS of $MnFe_2O_4$ nanoparticles

$NiFe_2O_4$

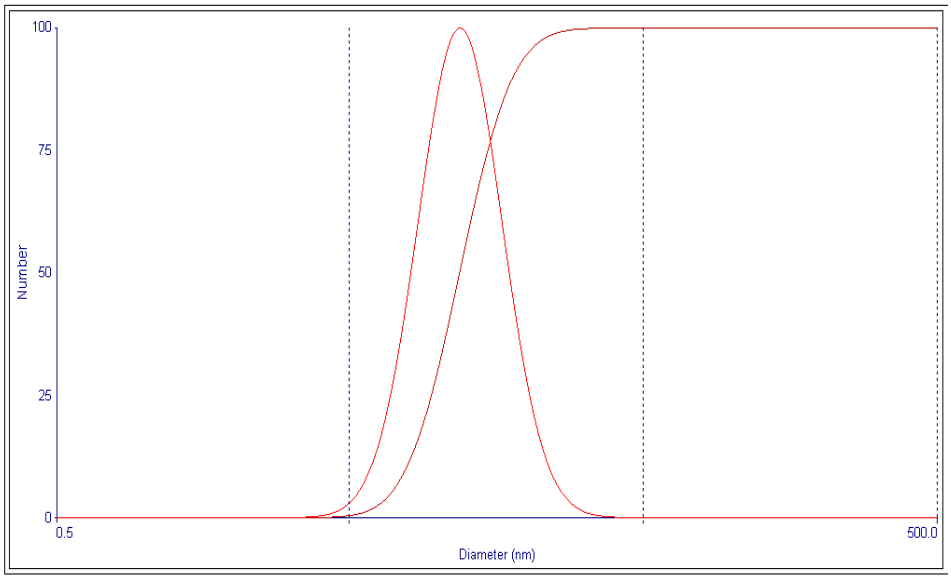

Figure 4.8: DLS of $NiFe_2O_4$ nanoparticles

Table 3: Particle size and polydispersity index calculated from DLS

S.No	Sample Specification	Particle size (nm)	Polydispersity Index
1.	Fe_3O_4	23.5	0.036
2.	$MnFe_2O_4$	22.0	0.065
3.	$NiFe_2O_4$	21.4	0.133

4.5 Conclusions

- ❖ Magnetic nanoparticles of Fe_3O_4, $NiFe_2O_4$ and $MnFe_2O_4$ have been prepared by chemical co-precipitation method.
- ❖ X-ray diffraction study confirms the cubic inverse spinel structure of Fe_3O_4, $MnFe_2O_4$, $NiFe_2O_4$. The broadening of peaks indicates that the as-synthesized samples have smaller sizes. The average crystallite size of the Fe_3O_4, $MnFe_2O_4$, $NiFe_2O_4$ nanoparticles are 8.40 nm, 9.06 nm and 8.25 nm, respectively.

- TEM study reveals that the Fe_3O_4 nanoparticles are polydisperse with nearly spherical morphology. The average size of the nanoparticles is 7 – 18 nm with polydispersity of 0.3.
- From the study of UV-visible spectrum, the band gaps of nanoparticles were determined. The band gap values for Fe_3O_4, $MnFe_2O_4$, $NiFe_2O_4$ are 3.03, 3.58 and 4.56, respectively.
- DLS analysis shows that the particle size of Fe_3O_4, $MnFe_2O_4$, $NiFe_2O_4$ nanoparticles comes out to be 23.5 nm, 22.0 nm and 21.4 nm, respectively and the polydispersity indices are 0.036, 0.065 and 0.133, respectively.

References

1. Luisa filipponi and Duncan Sutherland, Nanotechnology-brief introduction (2007).
2. N.Lane, J Nano.res.3 (2005)95.
3. Fritz Allhoff, Patrick Lin, Daniel Moore, John Wiley and Sons, (2010).
4. Lubick N, Environ Sci Techno 42 (11) :(2008) 3910.
5. Ron Kurtus,"basics of Magnetism" (2012).
6. Catherine Westbrook, Carolyn Kaut, Carolyn Kaut-Roth, MRI (Magnetic Resonance Imaging) in practice (2 ed.). Wiley-Blackwell (1998) p. 217
7. http://www.doitpoms.ac.uk/tlplib/ferromagnetic/types.php.
8. P.Kameli, magnetism of nanoscale particles, (2009).
9. X. Batlle, A. Labarta, J. Phys. D (2002), 35, R15.
10. R. H. Kodama, J. Magn. Mater. *(*1999), 200, 359.
11. P.W Anderson Phys. Rev., 79 (1950), p. 350
12. R.H Kodama, A.E Berkowitz, E.J McNiff Jr., S Foner Phys Rev. Lett., 77 (1996), p. 394
13. http://askville.amazon.com/meaningsuperparamagnetism/AnswerViewer.do?requestId=2899101
14. Carter, C. Barry; Norton, M. Grant "Ceramic materials: science and engineering" Springer, (2007) ISBN 0-387-46270-8
15. J. L. Snoek, Elsevier Publishing Co., Inc., New York-Amsterdam, (1947).
16. Gary Wulfsberg, Inorganic Chemistry, University Science Books (2000) 691.
17. Modern Ferrite Technology: Crystal structures of Ferrites, 52-69.
18. K. Parvin, J. Ma, and J. Ly,X. C. Sun and D. E. Nikles,K. Sun and L. M. Wang ,Volume 95, 2004.
19. Jing Sun, Shaobing Zhou, Peng Hou,Yuan Yang, Jie Weng,Xiaohong Li, Mingyuan Li, (2006).
20. Shen Wu , Aizhi Sun , Fuqiang Zhai, Jin Wang , Wenhuan Xu, Qian Zhang , Alex A. Volinsky, Materials Letters 65 (2011) 1882–1884.
21. Eunae Kang,Jongnam Park,Yosun Hwang, Misun Kang, Je-Geun Park, and Taeghwan Hyeon, J. Phys. Chem. B (2004), 108, 13932-13935.
22. C. N. Chinnasamy, Aria Yang, S. D. Yoon, and Kailin Hsu, M. D. Shultz and E. E. Carpenter, S. Mukerjee,C, C. Vittoria and V. G. Harris, Journal of Applied Physics 101, 09M509 (2007).
23. Mortaza Mozaffari, Behshid Behdadfar, Jamshid Amighian, Iranian Journal of

Pharmaceutical Sciences Spring (2008): 4(2): 115-118.

24. Yasir Jamil, M. Raza Ahmad, Abdul Hafeez, Zia ul Haq and Nasir Amin, Pak. J. Agri. Sci., Vol. 45(3), 2008.

25. Kurikka V. P. M. Shafi, Yuri Koltypin, and Aharon Gedanken, Ruslan Prozorov, Judit Balogh, Janos Lendvai, Israel Felner, J. Phys. Chem. B 1997, 101, 6409-6414.

26. Z. H. Zhou, J. M. Xue, and J. Wang,H. S. O. Chan,T. Yu and Z. X. Shen, Journal of Applied physics, volume 91, 2002.

27. Kamellia Nejati and Rezvanh Zabihi, Chemistry Central Journal 2012.

28. Patnaik, P. Dean's Analytical Chemistry Handbook, 2nd ed. McGraw-Hill, 2004.

29. Harvey, D. Modern Analytical Chemistry. McGraw-Hill, 2000.

30. A.H. Lu, E. L. Salabas and F. Schüth, Angew. Chem., Int. Ed., 2007, 46, 1222–1244.

31. G.Gnanaprakash, S.Ayyappan, T.Jayakumar, John Philip & Baldev Raj (2006), Nanotechnology 17: 5851–5857.

32. G. Gnanaprakash, John Philip, T. Jayakumar, Baldev Raj (2007), J. Phys. Chem. B 111: 7978–7986

33. S.Ayyappan, John Philip & Baldev Raj (2009), J. Phys. Chem. C 113: 590–596.

34. S. Ayyappan, S. Mahadevan, P. Chandramohan, M. P.Srinivasan, John Philip & Baldev Raj (2010), J. Phys. Chem. C 114: 6334–6341.

35. Bragg W.L. Proceedings of the Cambridge Philosophical Society (1913). **17**: 43–57.

36. O'Keefe MA, Allard LF (pdf). Sub-Ångstrom Electron Microscopy for Sub-Ångstrom Nano-Metrology. Information Bridge: DOE Scientific and Technical Information – Sponsored by OSTI (2010).

37. B D Cullity, Elements of X-ray diffraction, Addison-Wesley pub. Co (1978)

38. http://en.wikipedia.org/wiki/Planck_constant

39. N Andhariya, B Chudasama, R V Mehta, R V Upadhyay, J. Nanoparticle Research 13(2011) 1677.

40. Ulf Nobbmann, Malcolm Connah, Brendan Fish, Paul Varley, Chris Gee, Sandrine Mulot, Juntao Chen, Liang Zhou, Yanling Lu, Fei Sheng, Junming Yi and Stephen E. Harding, Vol. 24, 117-128 (2007).

41.http://ucordova.squarespace.com/blog/2011/11/10/dynamic-light-scatteringdls-diffusivity-calculations.html.